PCCP

ROYAL SOCIETY OF CHEMISTRY

PAPER

View Article Online
View Journal

Check for updates

Cite this: DOI: 10.1039/d6cp01673a

Mechanistic insights into room–temperature phosphorescence in a 1,4-diiodotetrafluorobenzene–phenanthrene cocrystal

K. Rueangboon, M. E. Sandoval-Salinas * and R. Crespo-Otero *

Received 6th May 2026,
Accepted 19th June 2026

DOI: 10.1039/d6cp01673a

rsc.li/pccp

Room-temperature phosphorescent (RTP) organic materials are attracting increasing interest for applications in optoelectronics, sensing, photomedicine, bioimaging, and OLED technologies. Metal-free organic emitters are particularly appealing due to their low toxicity, tunable photophysics, and reduced cost compared with organometallic systems. Recent work by Abe *et al.* (*Adv. Mater.* 2024, **36**, 2211160) demonstrated that cocrystals composed of 1,4-diiodotetrafluorobenzene (DITFB) and phenanthrene (Phen) exhibit efficient RTP, yet the microscopic mechanisms enabling this behaviour remain unclear. Here, we investigate the radiative and non-radiative excited-state processes in the **Phen–DITFB** system using an embedded multiscale approach to elucidate the factors governing RTP in organic cocrystals. Our results show that cocrystallisation profoundly reshapes the excited-state landscape relative to the isolated molecules. Aggregation increases the density of triplet states near the lowest singlet excited state (S_1), creating multiple energetically accessible ISC channels (T_4–T_{10}). Spin–orbit couplings are simultaneously enhanced through both intermolecular and, in specific cases, intramolecular charge-transfer contributions. The resulting triplet manifold displays a diversity of electronic characters: several states are localised on the DITFB units, enabling intermolecular charge-transfer-assisted $S_1 \rightarrow T_n$ transitions, while T_9 shows intramolecular electron reorganisation on Phen that further strengthens the SOC. This interplay between localisation, CT character, and orbital composition produces highly efficient ISC pathways, as confirmed by the computed rate constants. Collectively, these findings provide a detailed mechanistic picture of RTP in the **Phen–DITFB** cocrystal. Cocrystallisation enhances RTP by increasing the density of accessible triplet states, strengthening SOC through CT-mediated interactions, and suppressing competing non-radiative decay pathways. This study highlights how molecular electronic structure and supramolecular organisation act synergistically to enable efficient RTP in purely organic systems.

1. Introduction

Room-temperature phosphorescence (RTP) materials emit light after the excitation source is removed, even at ambient conditions.[1] Traditional RTP systems often rely on organometallic compounds, but metal-free organic molecules have emerged as a promising alternative.[2,3] These organic phosphors offer advantages such as lower toxicity, greater molecular tunability, and reduced production costs,[4] making them particularly appealing for applications in optoelectronics, sensing, photomedicine, bioimaging, OLEDs, and solar cells.[5,6]

The inherently low spin–orbit couplings (SOCs) in metal-free organic materials, together with the prevalence of competitive nonradiative and radiative pathways, result in small triplet populations and low phosphorescence rates. These factors have been identified as major limitations in improving RTP efficiency. Strategies developed to overcome these challenges include the incorporation of heteroatoms, particularly nonmetals such as iodine,[7–9] and Group 16 elements (S, Se),[10] to enhance SOCs,[7,8,11] the promotion of aggregate-induced intersystem crossing (ISC),[12–14] and the stabilisation of charge-transfer mechanisms.[15] Additionally, tuning the environment can suppress competing deactivation pathways while also limiting oxygen diffusion, thereby preventing oxygen quenching and other nonradiative processes.[16]

Cocrystallisation has recently emerged as an effective strategy to create a triplet manifold near the S_1 excited state, enabling multiple ISC channels and enhancing phosphorescence efficiency.[17–19] Different intermolecular interactions, such as hydrogen bonding, halogen bonding, and electrostatic forces, can modulate ISC. During ISC, electron transfer can be

---

*Department of Chemistry, University College London, London WC1H 0AJ, UK.
E-mail: m.salinas@ucl.ac.uk, r.crespo-otero@ucl.ac.uk*

facilitated through a charge-transfer (CT) state, which narrows the energy gap between the first singlet excited state and the triplet manifold ($\Delta E_{S_1T_n}$). A recent study by Abe *et al.* explored these principles to enhance RTP efficiency.[20] They investigated a series of cocrystals formed between 1,4-diiodotetrafluorobenzene (DITFB) and polyaromatic hydrocarbons, including phenanthrene (Phen), chrysene, and pyrene. Their work showed that halogen bond interactions play a crucial role in determining the phosphorescence quantum yield (Φ_P). The 1 : 2 **Phen–DITFB** cocrystal, dominated by σ–π intermolecular interactions, exhibits a significantly higher Φ_P than other binary cocrystals that rely on π–π stacking interactions.

In this paper, we investigate the mechanisms governing excited-state relaxation in the **Phen–DITFB** cocrystal, which serves as a representative model for organic cocrystals exhibiting RTP. Our protocol examines the excited states of both isolated molecules to rationalise the effects of aggregation. Potential Energy Surfaces (PES), spin–orbit couplings (SOCs), and the rates of various radiative and nonradiative pathways were computed using an embedded approach to incorporate environmental effects. Our calculations show that aggregation increases the density of states with different spin multiplicities, directly influencing SOCs and ISC rates, while the restricted molecular motions imposed by the crystal suppress competing deactivation pathways. These insights contribute to a more comprehensive understanding of RTP mechanisms in purely organic cocrystals.

2. Computational details

The structure of the **Phen–DITFB** cocrystal was obtained from the Cambridge Structural Database (CCDC 2220369) as reported by Abe *et al.*[20] This structure was refined using periodic DFT with a plane-wave basis set, as implemented in the Vienna *Ab initio* Simulation Package (VASP) version 5.4.4.[21] The PBEsol functional,[22] including D3 dispersion correction,[23] a plane-wave basis set kinetic energy cut-off to 400 eV and a 6 × 3 × 3 *k*-point grid were employed.

To study the excited-state mechanisms in this cocrystal, we employed the electrostatic embedding ONIOM(QM:QM’) scheme implemented in the *fromage* platform,[24,25] following a protocol previously shown to accurately describe solid-state photophysics.[2,3,26–30] A spherical cluster of approximately 30 Å radius was constructed, and a trimer consisting of two parallel DITFB molecules and one perpendicularly oriented Phen molecule was chosen as the basic unit for the QM region (Fig. 1). This trimer was selected due to the short intermolecular distances and the likelihood of relevant interactions contributing to the RTP mechanism. All remaining molecules in the cluster were assigned to the QM’ region.

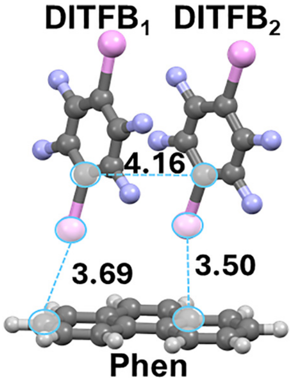

Fig. 1 Representative structure of the **Phen–DITFB** cocrystal. Pink, purple, grey, and white represent I, F, C, and H atoms, respectively. The shortest distances between monomers are shown in Å.

The QM region was treated using the ωB97X-D functional[31] and the SVP basis set,[32] and the corresponding time-dependent version within the Tamm–Dancoff approximation (TDA).[33] The QM’ region was described using the semi-empirical DFT tight-binding approach (DFTB).[34] Geometry optimisations of the FC, S_1, and T_1 states were carried out using the QM/QM’ scheme to incorporate environmental effects.

Excited-state properties of the lowest singlet and triplet states were further evaluated at the TDA-ωB97X-D/TZVP[35] and ADC(2)/SVP[36] levels of theory. For comparison, calculations on isolated monomers were also performed using TDA-ωB97X-D/SVP, TDA-ωB97X-D/TZVP, ADC(2)/SVP, and Mixed-Reference Spin–Flip TD-DFT (MRSF-TDDFT), which accounts for contributions from double excitations.[37] The MRSF-TDDFT calculations employed a Restricted Open-Shell (ROHF) triplet reference and were carried out with the B3LYP[38–40] and ωB97X-D functionals in combination with the TZVP basis set. Solvent effects were examined using single-point calculations at the TDA-B3LYP/TZVP and TDA-ωB97X-D/TZVP levels within the polarizable continuum model (PCM),[41] using benzene (ε = 2.27) and dichloromethane (ε = 8.93) as solvents. All calculations were performed as single points on the FC-optimised geometries of Phen and DITFB obtained at the ωB97X-D/SVP level. Geometry optimisations and TDA calculations were carried out with Gaussian16 Revision A.03,[42] MRSF-TDDFT calculations with Open-QP,[37,43] and ADC(2) calculations with Turbomole version 6.5.[44] The use of multiple levels of theory ensures the robustness and reliability of the results by reducing the likelihood that the conclusions are biased by methodological artefacts. In particular, ωB97X-D was selected for TDDFT calculations due to its reliable description of charge-transfer states and intermolecular interactions. Although the dispersion correction in wB97X-D does not modify the electronic structure, orbitals, or densities, it does influence the interaction energies of both ground and excited states and therefore affects the optimised geometries of both. While ADC(2) and MRSF-TDDFT were employed to validate excited-state properties and assess the role of electron correlation effects and double excitations. For all DFT calculations, the default numerical integration grids implemented in Gaussian and ORCA were used. Similarly, SCF convergence was achieved using the standard criteria in each code.

To investigate the ISC mechanism, spin–orbit coupling (SOC) values were computed at the TDA–ωB97X-D/SVP level of theory using the Breit–Pauli (BP) approximation, as implemented in

PySOC.[45] The nature of the excitations and the interactions among the three chromophores in the QM region were analysed using the TheoDore code,[46] following a fragment-based analysis of the one-electron transition density matrix (1TDM), in which each molecule was defined as a fragment (DITFB$_1$, DITFB$_2$, and Phen).

The fluorescence rate was calculated using the Einstein spontaneous emission expression (eqn (1)):

$$k_{\rm F}=\frac{\eta^2 f\Delta E_{ij}{}^2}{1.499} \tag{1}$$

where ΔE_{ij} is the vertical emission from the initial (i) to the final (j) state, specifically from S_1 to S_0 (in cm^{-1}), computed at the equilibrium geometry of S_1, and f is the oscillator strength. η is the refractive index of the crystal; here, the refractive index of pure phenanthrene (1.59) was used due to the absence of experimental data for the cocrystal.[47]

The ISC rate ($k_{\rm ISC}$) was modelled by considering SOC(S_1/T_n). Using the Born–Oppenheimer and Condon approximations derived from Fermi's Golden Rule (FGR), the ISC rate is expressed as (eqn (2)):[48]

$$k_{\rm ISC}=\frac{2\pi}{\hbar}({\rm SOC}(S_1/T_n))^2\sqrt{\frac{1}{4\pi\lambda k_{\rm B}T}}\exp\left(-\frac{(\Delta E_{ij}+\lambda)^2}{4\lambda k_{\rm B}T}\right) \tag{2}$$

where ΔE_{ij} is the adiabatic energy difference between the initial state (S_1 at its minimum-energy geometry) and the final state (T_n evaluated at the T_1 minimum). $\hbar$ is the reduced Planck constant, $k_{\rm B}$ is the Boltzmann constant, T is the temperature, and λ is the reorganisation energy.

The internal conversion (IC) rate was computed using the adiabatic model in its time-dependent formulation as implemented in FCclasses3:[49,50]

$$k_{\rm IC}=\frac{2\pi}{\hbar}\sum_{\nu_i\nu_f}P_{i\nu_i}(T)\left|\langle\mathbf{v}_i|\boldsymbol{\Lambda}^{if}\nabla_Q|\mathbf{v}_f\rangle\right|^2\delta\left(E_{i\nu_i}-E_{f\nu_f}\right) \tag{3}$$

where E_ν corresponds to the vibrational energies of the initial and final states, $\boldsymbol{\Lambda}^{if}$ are the nonadiabatic coupling elements, and $\nabla_Q=\sum_{k=1}^{N_{\rm vib}}\frac{\delta}{\delta Q_k}e_k$ is the vibrational displacement operator. A vibrational analysis at the equilibrium structures of both states is required.

The phosphorescence rate ($k_{\rm P}$) was computed under the zero-field splitting (ZFS) approximation. For each T_1 sublevel (a = 1–3), a corresponding $k_{{\rm P}_a}$ value was obtained using eqn (4):[51]

$$k_{{\rm P}_a}=\frac{1}{\tau_{{\rm P}_a}}=\frac{4\eta^2\Delta E^3_{ij(a)}}{3c^3}\sum_{b\in\{x,y,z\}}|\mu_{ij(a)}|_b^2 \tag{4}$$

where b denotes the component of the transition dipole moment, and SOC-corrected excited-state properties were computed using Orca version 5.0.4.[52] $\Delta E_{ij(a)}$ is the vertical T_1–S_0 energy gap at the T_1 geometry, and c is the speed of light in atomic units.[53]

The global phosphorescence lifetime ($\tau_{\rm P}$) was then obtained from the Boltzmann-weighted contributions of the three substates of the SOC-corrected triplets (m_s = −1,0,1), as shown in eqn (5):[51]

$$\tau_{\rm P}=\left(\frac{1+e^{-\Delta E_{1,2}/k_{\rm B}T}+e^{-\Delta E_{1,3}/k_{\rm B}T}}{k_{{\rm P}_1}+k_{{\rm P}_2}e^{-\Delta E_{1,2}/k_{\rm B}T}+k_{{\rm P}_3}e^{-\Delta E_{1,3}/k_{\rm B}T}}\right) \tag{5}$$

3. Results and discussion

3.1. Isolated molecules

3.1.1. Excited state energies. To establish a reference and evaluate the effect of crystallisation, we computed the gas-phase monomers at the TDA-ωB97X-D/SVP, TDA-ωB97X-D/TZVP, and ADC(2)/SVP levels of theory. The excitation energies of the lowest seven singlet and triplet states at the FC, S_1, and T_1 geometries of DITFB and Phen are shown in Fig. 2 and 3, with numerical values reported in Table S3. Additional TDA-ωB97X-D/TZVP calculations using the PCM model with benzene and CH_2Cl_2 were performed to assess solvent effects. To probe possible multireference character and contributions from double excitations, we also carried out MRSF-TDDFT calculations with the ωB97X-D and B3LYP functionals and the TZVP basis set. The corresponding excitation energies, including those obtained with implicit solvation, are listed in Tables S1 and S2.

For DITFB, the brightest excited state at the FC geometry is consistently S_7 (around 5.6 eV) across the TDA-ωB97X-D and ADC(2) methods (Fig. S1). Overall, the energetic ordering and state character are well reproduced at all geometries. Calculations with TDA-ωB97X-D using the two basis sets show only small variations, with standard deviations of approximately 0.10 eV. The agreement between TDA-ωB97X-D and ADC(2)

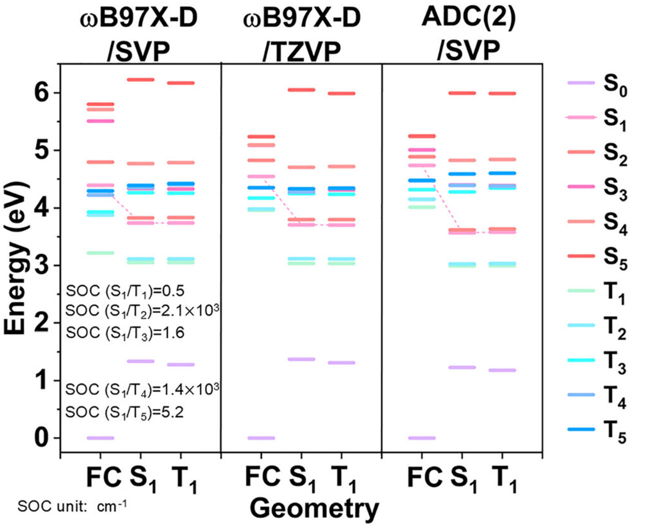

Fig. 2 Vertical excitation energy of isolated DITFB at FC, S_1, and T_1 geometries. The energy of S_1 is connected by pink dashed lines at the different minima. Computed at the TDA-ωB97X-D/SVP, TDA-ωB97X-D/TZVP, and ADC(2)/SVP levels of theory. The nonzero SOC values (cm^{-1}) are shown at the bottom, approximated at the S_1 geometry with the TDA-ωB97X-D/SVP level of theory.

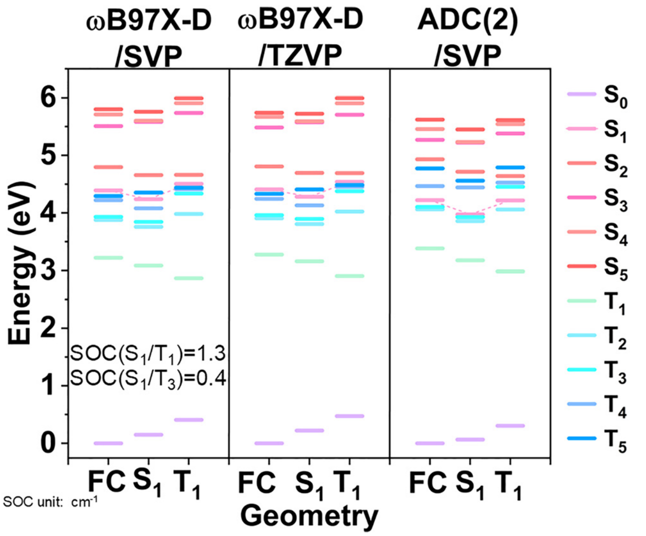

Fig. 3 Vertical excitation energy of isolated Phen at FC, S_1, and T_1 geometries. The energy of S_1 is connected by pink dashed lines at the different minima. Computed at the TDA-ωB97X-D/SVP, and ADC(2)/SVP levels of theory. The nonzero SOC values (cm^{-1}) are shown at the bottom, approximated at the S_1 geometry with the TDA-ωB97X-D/SVP level of theory.

for the same basis set is similarly good, with standard deviations around 0.14 eV. The largest deviation between TDA-ωB97X-D and ADC(2) occurs for the T_5 state (about 0.3 eV), while the largest difference within TDA-ωB97X-D appears for S_5 at the T_1 geometry (0.22 eV). These comparisons confirm that all levels of theory employed provide consistent excitation energies.

For DITFB, the calculated absorption energies in different solvents, including hexane and CH_2Cl_2, show only minimal changes (less than 0.10 eV at the ωB97X-D level), indicating weak solvent effects. The predicted absorption peak in CH_2Cl_2 agrees reasonably well with experiment: the measured value is 5.12 eV,[54] while the ωB97X-D calculations yield 5.44 eV in CH_2Cl_2 and 5.52 eV in benzene. The small differences between MRSF-TD-ωB97X-D and TDA excitation energies further indicate that contributions from double excitations are minor for the low-lying states, supporting a predominantly single-reference description (Table S2).

For isolated Phen, comparison of the excited-state energies obtained with TDA-ωB97X-D/TZVP relative to TDA-ωB97X-D/SVP yields standard deviations of 0.05 eV and 0.23 eV for the singlet and triplet manifolds, respectively. Although the deviations obtained with ADC(2) are larger than those observed for DITFB, all levels of theory still provide a consistent qualitative description of the photophysical behaviour of Phen. As in the case of DITFB, the excitation energies display only weak solvent dependence. MRSF-TD-ωB97X-D predicts the S_1 state at 4.44 eV, in good agreement with the TDA-based results and without any reordering of the low-lying states. At the ωB97X-D level, the S_1 state is found at 4.36 eV in both benzene and CH_2Cl_2, while S_2 is computed at 4.72 eV and 4.68 eV, differing by only 0.04 eV. Even for higher states, the variations remain modest; for example, S_3 shifts from 5.35 eV in benzene to 5.18 eV in CH_2Cl_2, corresponding to a maximum deviation of 0.17 eV. When compared with the experimental S_1 peak, which ranges from 3.58 eV in hexane[55] to 4.20 eV in cyclohexane,[56] the calculated S_1 energies (3.80–4.44 eV) are overestimated by approximately 0.22–0.24 eV (Table S1).

3.1.2. Single–triplet transitions. Near the S_1 minimum, only a few triplet states lie energetically close (Fig. 2 and 3). Because relaxation to S_1 is expected to be fast, we focus our analysis on the SOCs relevant for ISC between S_1 and the triplet manifold. Owing to the heavy-atom effect introduced by iodine, the spin–orbit couplings (SOCs) in DITFB are significantly larger than those in Phen. At the TDA-ωB97X-D/SVP level, the Phen monomer exhibits only two non-zero SOC values among the S_1/T_{1-5} manifold, namely S_1/T_1 (1.3 cm^{-1}) and S_1/T_3 (0.4 cm^{-1}). In contrast, DITFB shows non-zero SOCs for all corresponding transitions, with the largest value reaching 2073 cm^{-1} for S_1/T_2 (Table S4).

The electron density differences between the excited and ground states for each transition are shown in Fig. 4. For DITFB, the $S_1 \leftarrow S_0$ excitation corresponds to an electron redistribution from the in-plane region of the I atom to the out-of-plane region,

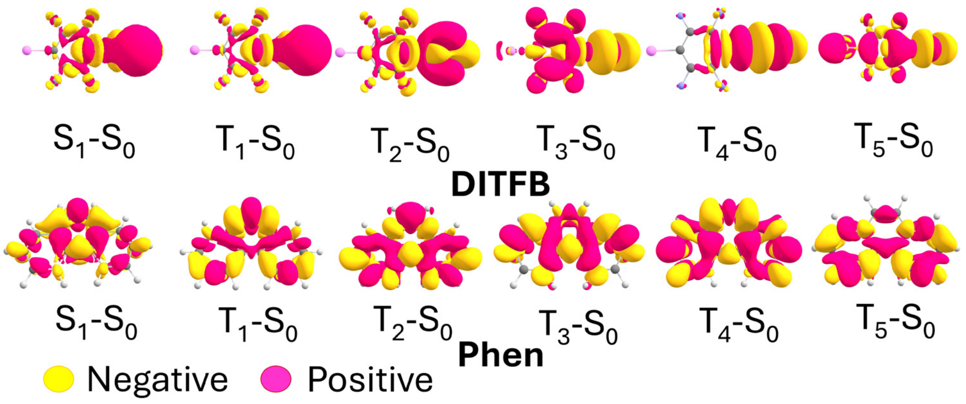

Fig. 4 Electronic density differences of S_1–S_0 and T_{1-5}–S_0 transitions of DITFB (top) and Phen (bottom) in the gas phase at the S_1 geometry. Computed at the TDA-ωB97X-D/SVP level of theory. Yellow and pink represent negative and positive isovalues, respectively.

consistent with a σ–π* transition. The T_1 state is characterised by a similar redistribution, while in $T_2 \leftarrow S_0$ the electron density remains localised in the molecular plane. For $T_4 \leftarrow S_0$, the density is mainly localised on the σ C–I bond, whereas in T_3 and T_5 the electron density shifts from the σ C–I bond toward the π* C–C bonds in the aromatic ring.

Electronic transitions $S_1 \leftarrow S_0$, $T_2 \leftarrow S_0$, and $T_4 \leftarrow S_0$ give rise to distinct electron density distributions which, according to El-Sayed's rule,[57] favour efficient ISC from S_1 to T_2 and T_4. The corresponding SOC values for the S_1/T_2 and S_1/T_4 couplings are 2.1×10^3 and 1.4×10^3 cm^{-1}, respectively. A similar analysis for Phen shows that most relevant transitions retain π–π* character, as expected for an unsubstituted polyaromatic hydrocarbon, resulting in minimal changes in electron density between states. The S_1–T_n energy gaps in DITFB are also considerably larger than those in Phen (Fig. 2 and 3), further contributing to their distinct photophysical behaviour.

Notably, efficient RTP cocrystals incorporating DITFB have been reported when paired with carbazole,[58] naphthalene,[59] and in piezochromic DITFB crystals, where high pressure enhances SOC(S_1/T_1) and SOC(T_1/S_0), simultaneously promoting ISC and radiative decay.[60] In contrast, Phen exhibits only weak phosphorescence in solution, with low intensities and short lifetimes.[61,62] In the next sections, we discuss how interactions between these molecules in the solid state govern RTP in the cocrystal.

3.2. RTP in the cocrystal

We aim to elucidate how the monomers interact within the **Phen–DITFB** cocrystal and how these interactions shape the excited-state mechanisms underlying RTP. To this end, we analyse the vertical excitations, excited-state characters, SOC(S_1/S_0) values, and photophysical rates (IC, ISC, fluorescence, and phosphorescence) in the crystalline environment of the **Phen–DITFB** cocrystal.

3.2.1. Excited state mechanisms. Fig. 5 shows the energy landscape of the **Phen–DITFB** cocrystal, displaying the five lowest singlet and ten lowest triplet states at the FC, S_1, and T_1 geometries computed with TDA-ωB97X-D/SVP, TDA-ωB97X-D/TZVP, and ADC(2)/SVP. These results allow direct comparison with the gas-phase monomers and highlight the effects of aggregation. As noted earlier, methodological differences lead to only minor deviations and do not alter the overall excitation-energy trends (Tables S5 and S6). For clarity, the discussion here focuses on the TDA-ωB97X-D/SVP data. At this level of theory, the weak intermolecular interactions in the cocrystal appear as small shifts relative to the monomer excitation energies in the gas phase (<0.07 eV), and as pairs of quasi-degenerate states that remain nearly isoenergetic with the DITFB excitations (Tables S5 and S6).

Following Kasha's rule,[63] photoexcitation is followed by ultrafast IC to S_1, from which several deactivation pathways become accessible, including non-radiative IC to S_0, ISC to the triplet manifold, and radiative decay *via* fluorescence. Upon relaxation to the S_1 geometry, the electronic density localises on the Phen fragment (Fig. 6), accompanied by a slight contraction of the trimer due to shortened intermolecular distances. As shown in Fig. 5, the number of triplet states that are (quasi-)degenerate with S_1 is larger in the cocrystal than in the isolated monomers at the same point on the PES.

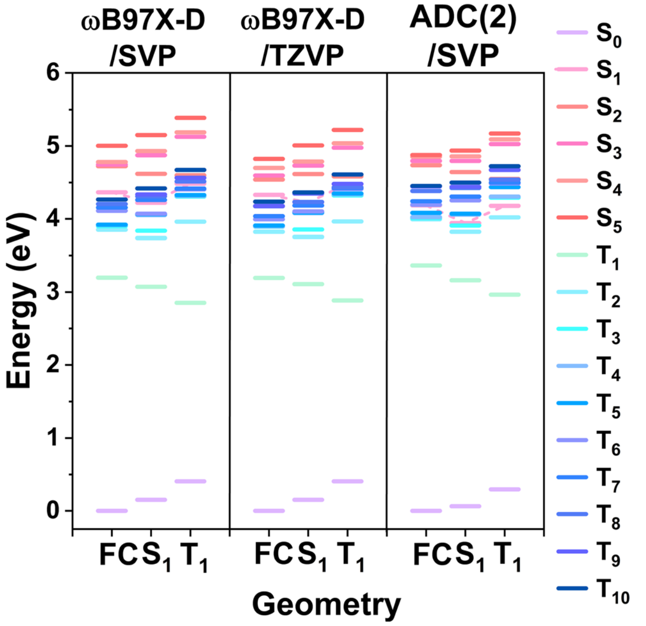

Fig. 5 Vertical excitation energies of the **Phen–DITFB** cocrystal at FC, S_1, and T_1 geometries. Computed at the TDA-ωB97X-D/SVP, TDA-ωB97X-D/TZVP, and ADC(2)/SVP levels of theory.

The S_1–T_n (n = 4–10) energy gaps range from 0.00 to 0.20 eV. These triplet states are mainly localised on the DITFB fragment or partially delocalised onto the Phen unit (Fig. 6), increasing the likelihood of ISC. Once in the triplet manifold, IC proceeds and the excitation relaxes to T_1, from which radiative decay (phosphorescence) can occur. In the next section, we assess the feasibility of ISC in **Phen–DITFB** by analysing the SOC values, the nature of the involved states, and the resulting non-radiative rates.

3.2.2. ISC: SOCs and CT characters. The transition between electronic states of different multiplicities, such as ISC from S_1 to the triplet manifold, is formally forbidden by spin conservation.[64] When treated as a perturbation, however, the SOC operator couples spin and orbital angular momenta, enabling the redistribution of angular momentum required for a singlet–triplet crossover. This interaction relaxes the spin-selection rule,[64] allowing ISC to occur as expressed in Eqn 2. Transitions involving a change in orbital type (*e.g.*, π → n* or n → π*) or between orbitals of similar type but different orientations further promote ISC by enhancing this redistribution.[57] The SOC values, $\Delta E_{S_1T_n}$ gaps, and electron localisations of the relevant T_n states in **Phen–DITFB** are summarised in Table 1. The discussion below focuses on the TDA-ωB97X-D/SVP results, which show good agreement with the other levels of theory.

In this system, the short intermolecular contacts within the cocrystal could favour the emergence of charge-transfer (CT) states, which may contribute to ISC through a mechanism analogous to Spin–Orbit Charge–Transfer Intersystem Crossing.[65,66]

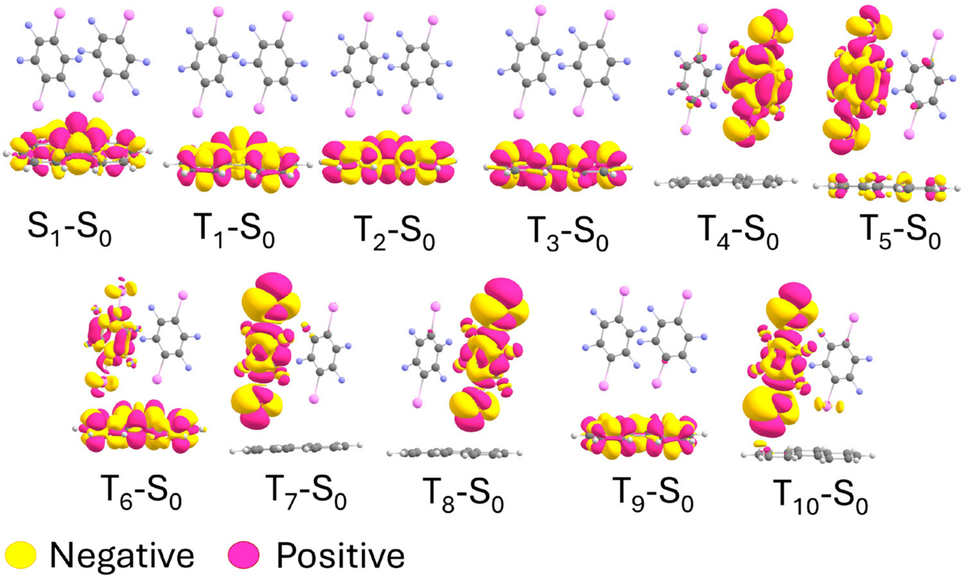

Fig. 6 Electron density differences of S_1–S_0 and T_{1-10}–S_0 transitions of the **Phen–DITFB** cocrystal at the S_1 geometry. Computed at the TDA-ωB97X-D/SVP level. Yellow and pink denote negative and positive isovalues, respectively.

Table 1 SOC values (cm^{-1}), energy gaps ($\Delta E_{S_1T_n}$, in eV), and character of the S_1–T_n transitions of the **Phen–DITFB** cocrystal at the S_1 geometry. Triplet states shown satisfy $\Delta E_{S_1T_n} < 0.20$ eV. Computed at the TDA-ωB97X-D/SVP level. $Char_{Tn}$ denotes the classification of each T_n state based on its main contributions in Fig. 7

	S_1/T_4	S_1/T_5	S_1/T_6	S_1/T_7	S_1/T_8	S_1/T_9	S_1/T_{10}
SOC	4.1	0.9	1.0	5.2	2.1	15.6	8.7
$\Delta E_{S_1T_n}$	0.18	0.17	0.16	0.03	0.00	−0.11	−0.13
$Char_{Tn}$	LC-$DITFB_2$	LC-$DITFB_1$	LC-Phen	LC-$DITFB_1$	LC-$DITFB_2$	LC-Phen	LC-$DITFB_1$

Since the S_1 state is largely localised on Phen, the nature of each T_n state determines whether the $S_1 \rightarrow T_n$ transition corresponds to an intermolecular or intramolecular charge redistribution. Multiple ISC channels become accessible from T_4 onward due to the small energy gaps (below 0.20 eV) combined with nonzero SOC values. The effect of cocrystallisation is particularly evident when comparing the SOCs of **Phen–DITFB** with those of isolated Phen. The latter exhibits only two S_1/T_n transitions with nonzero SOCs (maximum 1.3 cm^{-1}), whereas the cocrystal displays ten such transitions, including a pronounced 15.6 cm^{-1} SOC for S_1/T_9.

To clarify the origin of these couplings, Fig. 6 shows the electron density differences for the S_1–S_0 and T_n–S_0 transitions, while Fig. 7 provides a quantitative fragment-based analysis based on the three monomers ($DITFB_1$, $DITFB_2$, and Phen).[67] The five lowest singlet and triplet excited states are dominated by local (LC) excitations confined to individual molecules (Fig. 6 and 7). S_1, S_2, T_1, T_2, and T_3 are mainly localised on Phen, while S_3, S_5, and T_5 are centred on $DITFB_1$, and S_4 and T_4 on $DITFB_2$. All triplets localised on the DITFB units resemble the T_1 density of isolated DITFB. In isolated DITFB, T_1 shows the smallest SOC with S_1 (0.5 cm^{-1}). The larger SOCs observed here reflect the influence of aggregation.

In **Phen–DITFB**, T_4 lies 0.18 eV below S_1 (3.88 eV *vs.* 4.06 eV) with a SOC of 4.1 cm^{-1}. Its excitation is predominantly localised on $DITFB_2$ (89.32%) with a smaller contribution from $DITFB_1$ (9.13%). T_5 has a more mixed character (70.94% LC–$DITFB_1$, 7.92% LC–$DITFB_2$, and 19.55% LC–Phen) but exhibits a relatively small SOC (<1 cm^{-1}).

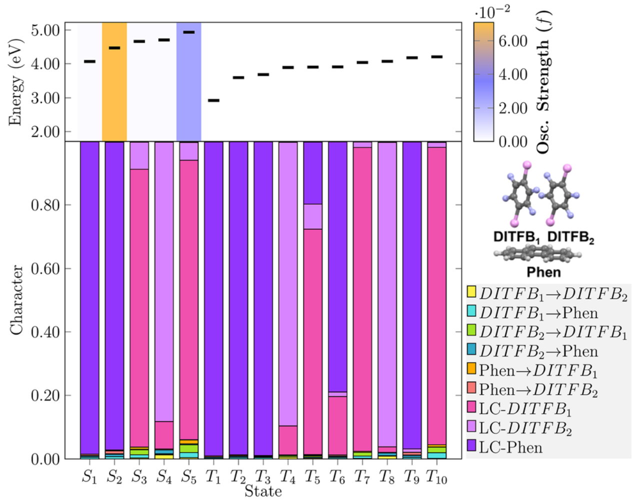

Fig. 7 Fragment-based analysis of the excited-state character of the **Phen–DITFB** cocrystal at the TDA-ωB97X-D/SVP level. The trimer is decomposed into three fragments: $DITFB_1$, $DITFB_2$, and Phen.

T_6 is dominated by LC–Phen (78.83%), with minor DITFB contributions and negligible CT components (below 0.40%). Its SOC is below 1 cm^{-1}. T_7, nearly isoenergetic with S_1 ($\Delta E \approx$ 0.03 eV), has a moderate SOC of 5.2 cm^{-1} and is mainly localised on $DITFB_1$ (95.7%) with small CT contributions (1.20% from $DITFB_2 \rightarrow DITFB_1$, 0.72% from $DITFB_1 \rightarrow$ Phen).

T_8 is nearly isoenergetic with S_1 and has an SOC of 2.1 cm^{-1}. It is strongly localised on $DITFB_1$ (95.85%) with smaller contributions from $DITFB_2$ (1.76%) and minor CT components. The S_1–T_9 gap is small (−0.11 eV), and T_9 is mostly localised on Phen (96.63%). The SOC of 15.6 cm^{-1}, the largest in this series, is consistent with both intermolecular CT contributions and pronounced intramolecular charge redistribution within Phen. In the $S_1 \rightarrow T_9$ transition, electron density shifts from the central aromatic ring to the outer rings. Mulliken charge analysis of T_9 reveals a slight positive charge on the central ring (approximately 0.1*e*), supporting this interpretation. T_{10} lies 0.13 eV below S_1 and exhibits the second-largest SOC (8.7 cm^{-1}). It is primarily localised on $DITFB_1$ (93.6%), with minor contributions from $DITFB_2$ (1.55%) and Phen (0.16%) and small CT components.

Overall, the triplet manifold near S_1 displays a diverse range of electronic characters. Several states are primarily localised on the DITFB units (T_4, T_5, T_7, T_8, T_{10}), and therefore the corresponding $S_1 \rightarrow T_n$ transitions involve intermolecular CT. By contrast, T_6 and T_9 are largely Phen-centered. In the case of T_9, both intermolecular CT and intramolecular reorganisation contribute to its enhanced SOC. This diversity illustrates how the interplay between localisation, charge-transfer components, and orbital character governs the intersystem crossing behaviour in the **Phen–DITFB** cocrystal. To fully understand the RTP mechanism, ISC rates between S_1 and the T_4–T_{10} manifold must therefore be evaluated and compared with the competing radiative and non-radiative decay pathways.

3.2.3. Calculation of rates.

To clarify the balance between radiative and non-radiative pathways, we computed the rates of the most relevant decay mechanisms in **Phen–DITFB**. Following the analysis of the previous section, particular attention was given to the ISC rates between S_1 and the T_n states, as these transitions govern the population of the triplet manifold in RTP. The corresponding rates in the crystalline environment are summarised in Table 2. Both fluorescence and $S_1 \rightarrow S_0$ internal conversion reduce the fraction of the S_1 population available for ISC.

The predicted fluorescence energy is 4.07 eV (305 nm), slightly blue-shifted relative to the Phen monomer (4.06 eV). The fluorescence rate $k_F = 5.45 \times 10^6$ s^{-1} was obtained using eqn (1). To describe the ISC process from S_1 to the triplet manifold, we evaluated the contributions of individual $S_1 \rightarrow T_n$ (n = 4–10) transitions. All of them exhibit large ISC rates in the range of 10^8–10^{10} s^{-1} (Table 2). The highest ISC rate is 7.42×10^{10} s^{-1} for the S_1/T_9 transition, consistent with its large SOC value as discussed in the previous section.

Another notable contribution is S_1/T_7, with a rate of 1.18×10^{10} s^{-1}, where an intermolecular ISC mechanism (Phen → DITFB) is plausible. Although T_{10} shows a larger SOC (8.7 cm^{-1}), the slightly larger energy gap (∼0.13 eV) yields a slower ISC rate of 8.43×10^9 s^{-1}. This comparison illustrates the balance between SOC magnitude and energy-gap factors in determining ISC efficiency.

To compare the contributions of all accessible pathways, we consider a global ISC rate constant:

$$k_{\mathrm{ISC}} = \sum_i k_{\mathrm{S_1T}_n}(i) \tag{6}$$

where the summation includes all energetically accessible triplet states close to S_1 at the S_1 geometry, namely T_4–T_{10}. For **Phen–DITFB**, the global ISC rate constant is $k_{ISC} = 9.93 \times 10^{10}$ s^{-1}. This rate is several orders of magnitude larger than k_F. Although the predicted internal conversion rate k_{IC} for the $S_1 \rightarrow S_0$ transition is based on the harmonic approximation and may underestimate the complexity of the process, its value remains much smaller ($k_{IC} = 3.07 \times 10^3$ s^{-1}). Together, these results indicate that population of the triplet manifold from S_1 is highly efficient in the **Phen–DITFB** cocrystal.

Once in the triplet manifold, rapid IC between triplet states and relaxation to the T_1 geometry are expected. Deactivation from T_1 to the ground state can proceed *via* radiative (phosphorescence) or non-radiative channels. The predicted phosphorescence emission energy is 2.45 eV, in reasonable agreement with the experimental value of 2.16 eV.[20] The predicted phosphorescence rate constant, $k_P = 2.15$ s^{-1}, is around one order of magnitude smaller than the experimental value of 35 s^{-1}. Given the approximations in the treatment of spin–orbit coupling, excitation energies, and the simplified representation of the solid-state environment, the level of agreement can be considered satisfactory. The experimental nonradiative decay rate for the

Table 2 Rates of competitive pathways in **Phen–DITFB** cocrystals, including radiative processes *via* fluorescence (k_F) and phosphorescence (k_P), as well as non-radiative processes such as internal conversion (k_{IC}) and intersystem crossing (k_{ISC}), all reported in s^{-1}. Radiative lifetimes, *i.e.*, fluorescence (τ_F) and phosphorescence (τ_P) are reported in s

k_F (s^{-1})	k_{ISC} (s^{-1})	k_{IC} (s^{-1})	k_P (s^{-1})	τ_F (s)	τ_P (s)
5.5×10^6	2.8×10^9 (S_1/T_4) 1.6×10^8 (S_1/T_5) 1.6×10^8 (S_1/T_6) 1.2×10^{10} (S_1/T_7) 1.7×10^9 (S_1/T_8) 7.4×10^{10} (S_1/T_9) 8.4×10^9 (S_1/T_{10}) 9.9×10^{10} (global k_{ISC})	3.1×10^3 (S_1/S_0)	2.15	8×10^{-7}	6×10^{-1}

$T_1 \rightarrow S_0$ transition is $0.59 \times 10^3\ s^{-1}$, confirming that nonradiative decay is the dominant, and most detrimental pathway, limiting the phosphorescence quantum yield to 6%.[20]

Overall, our simulations demonstrate that cocrystallisation has a marked effect on the excited states of **Phen–DITFB**, reshaping the competition between radiative and non-radiative decay pathways, facilitating population of the triplet states, and enabling phosphorescence.

4. Conclusions

In this work, we investigated the light-driven mechanisms governing the photophysics of the **Phen–DITFB** cocrystal by analysing a representative trimeric unit with a 2 : 1 DITFB:Phen ratio. By first examining the isolated molecules and benchmarking several levels of theory, we established a consistent qualitative description of their excited-state landscapes, providing a reference for assessing how aggregation reshapes the electronic structure. Upon crystallisation, the system undergoes a marked increase in the density of triplet states near S_1, together with a substantial enhancement of spin–orbit couplings relative to the isolated Phen molecule. These effects arise from the emergence of both intermolecular and, in some cases, intramolecular charge-transfer contributions.

The resulting triplet manifold exhibits a diverse range of electronic characters. Several states (*e.g.*, T_4, T_5, T_7, T_8, T_{10}) are predominantly localised on the DITFB units, such that transitions from a Phen-centred S_1 involve intermolecular charge transfer. Others, including T_6 and T_9, are largely Phen-centred; in the specific case of T_9, intramolecular reorganisation of the electron density further strengthens the SOC. This interplay between localisation, CT character, and orbital composition dictates the intersystem crossing behaviour in the cocrystal. To capture this complexity, ISC rates between S_1 and the T_4–T_{10} manifold were computed and compared with the competing radiative and non-radiative decay channels. The results reveal that the total ISC rate ($9.9 \times 10^{10}\ s^{-1}$) overwhelmingly dominates over fluorescence ($5.5 \times 10^6\ s^{-1}$), demonstrating that population transfer from S_1 to the triplet manifold is highly efficient.

Once in the triplet manifold, deactivation proceeds primarily through phosphorescence or non-radiative decay. The predicted phosphorescence rate constant ($2.15\ s^{-1}$), while underestimated relative to experiment, corresponds to a lifetime consistent with the long-lived emission observed experimentally. Likewise, the computed phosphorescence energy (2.45 eV) shows good agreement with the experimental value of 2.16 eV. Overall, these findings present a comprehensive mechanistic description of RTP in **Phen–DITFB**: aggregation increases the density of accessible triplet states, enhances SOC through CT-mediated interactions, and promotes highly efficient ISC, while the crystalline environment suppresses detrimental relaxation pathways. This synergy between molecular electronic structure and solid-state organisation underpins the observed room-temperature phosphorescence of the **Phen–DITFB** cocrystal.

Conflicts of interest

There are no conflicts to declare.

Data availability

Additional data, including results at different levels of theory, spin–orbit couplings, transition densities and intersystem crossing rates are provided in the supplementary information (SI). Supplementary information includes additional data at different levels of theory, including spin–orbit couplings, transition densities, and rates. See DOI: https://doi.org/10.1039/d6cp01673a.

Acknowledgements

The authors acknowledge the use of the UCL High Performance Computing Facilities Myriad@UCL and Kathleen@UCL. We also acknowledge use of the ARCHER UK National Supercomputing Service (EP/X035859/1) *via* the Materials Chemistry Consortium, and the Molecular Modelling Hub (MMM Hub) for computational resources, which is partially funded by EPSRC (EP/T022213/1). Funding from UK Research and Innovation under the UK Government's Horizon Europe funding guarantee (grant number EP/X020908/2) is gratefully acknowledged. The authors also thank the Development and Promotion of Science and Technology Talents (DPST) Project, Thailand, for providing a full PhD scholarship.

References

1 Q. Peng, H. Ma and Z. Shuai, Theory of Long-Lived Room-Temperature Phosphorescence in Organic Aggregates, *Acc. Chem. Res.*, 2021, **54**(4), 940–949.

2 J. Zhou, L. Stojanovic′, A. A. Berezin, T. Battisti, A. Gill, B. M. Kariuki, D. Bonifazi, R. Crespo-Otero, M. R. Wasielewski and Y.-L. Wu, Organic room-temperature phosphorescence from halogen-bonded organic frameworks: hidden electronic effects in rigidified chromophores, *Chem. Sci.*, 2021, **12**(2), 767–773.

3 L. Stojanovic, M. Dommett and R. Crespo-Otero, Origins of crystallisation-induced dual emission of terephthalic and isophthalic acid crystals, *Phys. Chem. Chem. Phys.*, 2025, **27**, 14469–14481.

4 M. Ji and X. Ma, Recent progress with the application of organic room-temperature phosphorescent materials, *Ind. Chem. Mater.*, 2023, **1**(4), 582–594.

5 W. Zhao, Z. He and B. Zhong Tang, Room-temperature phosphorescence from organic aggregates, *Nat. Rev. Mater.*, 2020, **5**(12), 869–885.

6 H. Xu, C. Runfeng, Q. Sun, W. Lai, Q. Su, W. Huang and X. Liu, Recent progress in metal–organic complexes for optoelectronic applications, *Chem. Soc. Rev.*, 2014, **43**, 3259–3302.

7 A. Malinge, S. Kumar, D. Chen, E. Zysman-Colman and S. Kéna-Cohen, Heavy Atom Effect in Halogenated mCP and

Its Influence on the Efficiency of the Thermally Activated Delayed Fluorescence of Dopant Molecules, *J. Phys. Chem. C*, 2024, **128**(3), 1122–1130.

8 S. P. McGlynn, R. Sunseri and N. Christodouleas, External Heavy-Atom Spin-Orbital Coupling Effect. I. The Nature of the Interaction, *J. Chem. Phys.*, 1962, **37**(8), 1818–1824.

9 Y. Yang, Q. Li and Z. Li, Advances in organic room-temperature phosphorescence: design strategies, photophysical mechanisms, and emerging applications, *Mater. Chem. Front.*, 2025, **9**(5), 744–753.

10 K. Shizu, Y. Ren and H. Kaji, Promoting Reverse Intersystem Crossing in Thermally Activated Delayed Fluorescence via the Heavy-Atom Effect, *J. Phys. Chem. A*, 2023, **127**(2), 439–449.

11 E. Lucenti, A. Forni, C. Botta, C. Giannini, D. Malpicci, D. Marinotto, A. Previtali, S. Righetto and E. Cariati, Intrinsic and Extrinsic Heavy-Atom Effects on the Multifaceted Emissive Behavior of Cyclic Triimidazole, *Chem. – Eur. J.*, 2019, **25**(10), 2452–2456.

12 L. Yang, X. Wang, G. Zhang, X. Chen, G. Zhang and J. Jiang, Aggregation-induced intersystem crossing: a novel strategy for efficient molecular phosphorescence, *Nanoscale*, 2016, **8**(40), 17422–17426.

13 X.-Y. Wang, J. Gong, H. Zou, S. Hua Liu and J. Zhang, Aggregation-induced conversion from TADF to phosphorescence of gold(I) complexes with millisecond lifetimes, *Aggregate*, 2023, **4**(2), e252.

14 J. You, X. Zhang, Q. Nan, K. Jin, J. Zhang, Y. Wang, C. Yin, Z. Yang and J. Zhang, Aggregation-regulated room-temperature phosphorescence materials with multi-mode emission, adjustable excitation-dependence and visible-light excitation, *Nat. Commun.*, 2023, **14**(1), 4163.

15 J. Fang, P. Li, X. Xue, H. Li, D. Cui, J. Zhang, Y. Wang, T. Debnath, Y. Jie, W. Huang and R. Chen, Realignment of Local and Charge-Transfer Excited States in Promoting Room-Temperature Phosphorescence of Organic Aggregates, *Chem. Mater.*, 2023, **35**(16), 6405–6414.

16 S. Hirata, K. Totani, J. Zhang, T. Yamashita, H. Kaji, S. R. Marder, T. Watanabe and C. Adachi, Efficient persistent room temperature phosphorescence in organic amorphous materials under ambient conditions, *Adv. Funct. Mater.*, 2013, **23**(27), 3386–3397.

17 W. Zhang Yuan, X. Yuan Shen, H. Zhao, J. W. Y. Lam, L. Tang, P. Lu, C. Wang, Y. Liu, Z. Wang, Q. Zheng, J. Zhi Sun, Y. Ma and B. Zhong Tang, Crystallization-Induced Phosphorescence of Pure Organic Luminogens at Room Temperature, *J. Phys. Chem. C*, 2010, **114**(13), 6090–6099.

18 Z. Xu, Y. He, H. Shi and Z. An, Room-temperature phosphorescence materials from crystalline to amorphous state, *SmartMat*, 2023, **4**(1), e1139.

19 Q. Jia, X. Yan, B. Wang, J. Li, W. Xu, Z. Shen, C. Bo, Y. Li and L. Chen, Construction of room temperature phosphorescent materials with ultralong lifetime by in-situ derivation strategy, *Nat. Commun.*, 2023, **14**(1), 4164.

20 K. Goushi, A. Abe, M. Mamada and C. Adachi, Organic binary and ternary cocrystal engineering based on halogen bonding aimed at room-temperature phosphorescence, *Adv. Mater.*, 2024, **36**(20), 2211160.

21 J. Hafner and G. Kresse, The Vienna AB-Initio Simulation Program VASP: An Efficient and Versatile Tool for Studying the Structural, Dynamic, and Electronic Properties of Materials, *In Antonios Gonis*, ed A. Meike, and P. E. A. Turchi, *Properties of Complex Inorganic Solids*, Springer US, Boston, MA, 1997, pp 69–82.

22 J. P. Perdew, A. Ruzsinszky, G. I. Csonka, O. A. Vydrov, G. E. Scuseria, L. A. Constantin, X. Zhou and K. Burke, Restoring the Density-Gradient Expansion for Exchange in Solids and Surfaces, *Phys. Rev. Lett.*, 2008, **100**(13), 136406.

23 T. Sandberg and P. Eklund, The effect of density functional dispersion correction (DFT-D3) on lignans, *Comput. Theor. Chem.*, 2015, **1067**, 60–63.

24 M. Rivera, M. Dommett and R. Crespo-Otero, ONIOM(QM:QM) Electrostatic Embedding Schemes for Photochemistry in Molecular Crystals, *J. Chem. Theory Comput.*, 2019, **15**(4), 2504–2516.

25 M. Rivera, M. Dommett, A. Sidat, W. Rahim and R. Crespo-Otero, Fromage: A library for the study of molecular crystal excited states at the aggregate scale, *J. Comput. Chem.*, 2020, **41**(10), 1045–1058.

26 F. J. Hernández and R. Crespo-Otero, Excited state mechanisms in crystalline carbazole: the role of aggregation and isomeric defects, *J. Mater. Chem. C*, 2021, **9**(35), 11882–11892.

27 A. Sidat, M. Ingham, M. Rivera, A. J. Misquitta and R. Crespo-Otero, Performance of point charge embedding schemes for excited states in molecular organic crystals, *J. Chem. Phys.*, 2023, **159**(24), 244108.

28 M. Ingham, M. Brady and R. Crespo-Otero, Describing excited states of covalently connected crystals with cluster and embedded cluster approaches: Challenges and solutions, *J. Chem. Theory Comput.*, 2025, **21**(15), 7576–7592.

29 A. Navarro-Huerta, A. Juárez-Calixto, M. Eugenia Sandoval-Salinas, Y. A. Amador-Sánchez, J. Rodrguez-Hernández, A. Núñez-Pineda, M. Rodrguez, R. Crespo-Otero and B. Rodrguez-Molina, Mechanochromic hydrogen-bonded cocrystals with a salient effect upon heating, *Mater. Chem. Front.*, 2024, **8**(20), 3331–3343.

30 K. Gorbatenko, E. Mendez-Vega, M. Eugenia Sandoval-Salinas, F. J. Hernández, R. Crespo-Otero and W. Sander, A magnetically bistable rigid carbene 2,3-benzofluorenylidene, *J. Am. Chem. Soc.*, 2026, **148**(15), 15883–15896.

31 C. Jeng-Da and M. Head-Gordon, Long-range corrected hybrid density functionals with damped atom–atom dispersion corrections, *Phys. Chem. Chem. Phys.*, 2008, **10**(44), 6615–6620.

32 A. Schäfer, H. Horn and R. Ahlrichs, Fully optimized contracted Gaussian basis sets for atoms Li to Kr, *J. Chem. Phys.*, 1992, **97**(4), 2571–2577.

33 S. Hirata and M. Head-Gordon, Time-dependent density functional theory within the Tamm–Dancoff approximation, *Chem. Phys. Lett.*, 1999, **314**(3), 291–299.

34 B. Aradi, B. Hourahine and T. Frauenheim, DFTB+, a Sparse Matrix-Based Implementation of the DFTB Method, *J. Phys. Chem. A*, 2007, **111**(26), 5678–5684.

35 F. Weigend and R. Ahlrichs, Balanced basis sets of split valence, triple zeta valence and quadruple zeta valence quality for H to Rn: Design and assessment of accuracy, *Phys. Chem. Chem. Phys.*, 2005, **7**(18), 3297–3305.

36 J. Schirmer, Beyond the random-phase approximation: A new approximation scheme for the polarization propagator, *Phys. Rev. A*, 1982, **26**(5), 2395–2416.

37 W. Park, K. Komarov, S. Lee and C. Ho Choi, Mixed-Reference Spin-Flip Time-Dependent Density Functional Theory: Multireference Advantages with the Practicality of Linear Response Theory, *J. Phys. Chem. Lett.*, 2023, **14**(39), 8896–8908.

38 C. Lee, Development of the Colle-Salvetti correlation-energy formula into a functional of the electron density, *Phys. Rev. B: Condens. Matter Mater. Phys.*, 1988, **37**(2), 785–789.

39 D. Axel, Becke. Density-functional thermochemistry. III. The role of exact exchange, *J. Chem. Phys.*, 1993, **98**(7), 5648–5652.

40 P. J. Stephens, F. J. Devlin, C. F. Chabalowski and M. J. Frisch, Ab initio calculation of vibrational absorption and circular dichroism spectra using density functional force fields, *J. Phys. Chem.*, 1994, **98**(45), 11623–11627.

41 J. Tomasi, B. Mennucci and R. Cammi, Quantum Mechanical Continuum Solvation Models, *Chem. Rev.*, 2005, **105**(8), 2999–3094.

42 M. J. Frisch, G. W. Trucks, H. B. Schlegel, G. E. Scuseria, M. A. Robb, J. R. Cheeseman, G. Scalmani, V. Barone, G. A. Petersson, H. Nakatsuji, X. Li, M. Caricato, A. V. Marenich, J. Bloino, B. G. Janesko, R. Gomperts, B. Mennucci, H. P. Hratchian, J. V. Ortiz, A. F. Izmaylov, J. L. Sonnenberg, D. Williams-Young, F. Ding, F. Lipparini, F. Egidi, J. Goings, B. Peng, A. Petrone, T. Henderson, D. Ranasinghe, V. G. Zakrzewski, J. Gao, N. Rega, G. Zheng, W. Liang, M. Hada, M. Ehara, K. Toyota, R. Fukuda, J. Hasegawa, M. Ishida, T. Nakajima, Y. Honda, O. Kitao, H. Nakai, T. Vreven, K. Throssell, J. A. Montgomery Jr., J. E. Peralta, F. Ogliaro, M. J. Bearpark, J. J. Heyd, E. N. Brothers, K. N. Kudin, V. N. Staroverov, T. A. Keith, R. Kobayashi, J. Normand, K. Raghavachari, A. P. Rendell, J. C. Burant, S. S. Iyengar, J. Tomasi, M. Cossi, J. M. Millam, M. Klene, C. Adamo, R. Cammi, J. W. Ochterski, R. L. Martin, K. Morokuma, O. Farkas, J. B. Foresman and D. J. Fox, *Gaussian 16, Rev. A.03*, 2016.

43 V. Mironov, K. Komarov, J. Li, I. Gerasimov, H. Nakata, M. Mazaherifar, K. Ishimura, W. Park, A. Lashkaripour, M. Oh, M. Huix-Rotllant, S. Lee and C. Ho Choi, OpenQP: A Quantum Chemical Platform Featuring MRSF-TDDFT with an Emphasis on Open-Source Ecosystem, *J. Chem. Theory Comput.*, 2024, **20**(21), 9464–9477.

44 S. Ganesh Balasubramani, G. P. Chen, S. Coriani, M. Diedenhofen, M. S. Frank, Y. J. Franzke, F. Furche, R. Grotjahn, M. E. Harding, C. Hättig, A. Hellweg, B. Helmich-Paris, C. Holzer, U. Huniar, M. Kaupp, A. Marefat Khah, S. Karbalaei Khani, T. Müller, F. Mack, B. D. Nguyen, S. M. Parker, E. Perlt, D. Rappoport, K. Reiter, S. Roy, M. Rückert, G. Schmitz, M. Sierka, E. Tapavicza, D. P. Tew, C. van Wüllen, V. K. Voora, F. Weigend, A. Wodynski and J. M. Yu, TURBOMOLE: Modular program suite for ab initio quantum-chemical and condensed-matter simulations, *J. Chem. Phys.*, 2020, **152**(18), 184107.

45 X. Gao, S. Bai, D. Fazzi, T. Niehaus, M. Barbatti and W. Thiel, Evaluation of Spin-Orbit Couplings with Linear-Response Time-Dependent Density Functional Methods, *J. Chem. Theory Comput.*, 2017, **13**(2), 515–524.

46 F. Plasser, M. Wormit and A. Dreuw., New tools for the systematic analysis and visualization of electronic excitations. I. Formalism, *J. Chem. Phys.*, 2014, **141**(2), 024106.

47 PubChem. Hazardous Substances Data Bank (HSDB): 2166.

48 Z. Zhao, H. Zhang, J. W. Y. Lam and B. Zhong Tang, Aggregation-induced emission: new vistas at the aggregate level, *Angew. Chem., Int. Ed.*, 2020, **59**(25), 9888–9907.

49 J. Cerezo and F. Santoro, FCclasses3: Vibrationally-resolved spectra simulated at the edge of the harmonic approximation, *J. Comput. Chem.*, 2023, **44**(4), 626–643.

50 L. Shi, X. Xie and A. Troisi, Rapid calculation of internal conversion and intersystem crossing rate for organic materials discovery, *J. Chem. Phys.*, 2022, **157**(13), 134106.

51 K. Mori, T. P. M. Goumans, E. Van Lenthe and F. Wang, Predicting phosphorescent lifetimes and zero-field splitting of organometallic complexes with time-dependent density functional theory including spin–orbit coupling, *Phys. Chem. Chem. Phys.*, 2014, **16**(28), 14523–14530.

52 F. Neese, F. Wennmohs, U. Becker and C. Riplinger, The ORCA quantum chemistry program package, *J. Chem. Phys.*, 2020, **152**(22), 224108.

53 W. Nau, Modern Molecular Photochemistry of Organic Molecules. by N. J. Turro, V. Ramamurthy, J. C. Scaiano, *Chem. Phys. Chem.*, 2011, **12**, 2496–2497.

54 C. Feng, S. Li, X. Xiao, Y. Lei, H. Geng, Y. Liao, Q. Liao, J. Yao, Y. Wu and H. Fu, Excited-state modulation for controlling fluorescence and phosphorescence pathways toward white-light emission, *Adv. Opt. Mater.*, 2019, **7**(20), 1900767.

55 Y. Nakamura, T. Tsuihiji, T. Mita, T. Minowa, S. Tobita, H. Shizuka and J. Nishimura, Synthesis, Structure, and Electronic Properties of syn-[2.2]Phenanthrenophanes: First Observation of Their Excimer Fluorescence at High Temperature, *J. Am. Chem. Soc.*, 1996, **118**(5), 1006–1012.

56 M. Yamaji, Y. Hakoda, A. Horimoto and H. Okamoto, Photochemical synthesis of diphenylphenanthrenes, and the photophysical properties studied by emission and transient absorption measurements, *Rapid Commun. Photosci.*, 2014, **3**, 73–75.

57 M. A. El-Sayed, Triplet state. Its radiative and nonradiative properties, *Acc. Chem. Res.*, 1968, **1**(1), 8–16.

58 H. Yue Gao, Q. Jin Shen, X. Ran Zhao, X. Qing Yan, X. Pang and W. Jun Jin, Phosphorescent co-crystal assembled by 1,4-diiodotetrafluorobenzene with carbazole based on C–I halogen bonding, *J. Mater. Chem.*, 2012, **22**(12), 5336–5343.

59 Q. Jin Shen, X. Pang, X. Ran Zhao, H. Yue Gao, H.-L. Sun and W. Jun Jin, Phosphorescent cocrystals constructed by 1,4-diiodotetrafluorobenzene and polyaromatic hydrocarbons

based on C–I halogen bonding and other assisting weak interactions, *CrystEngComm*, 2012, **14**(15), 5027–5034.

60 T. Xu, C. Zhai, Z. Liu, X. Yang, S. Hu, Y. Shang, L. Yue, J. Dong, R. Liu, Q. Li, M. Yao and B. Liu, Room-temperature phosphorescence and anomalous piezochromism in molecular crystals enabled by iodine atomic orbital sharing, *Nat. Commun.*, 2025, **16**(1), 3550.

61 S. Tean and Y. Gondo, Non-exponential phosphorescence decay of phenanthrene in biphenyl, *Chem. Phys. Lett.*, 1986, **123**(5), 441–444.

62 K. Kalyanasundaram, F. Grieser and J. K. Thomas, Room temperature phosphorescence of aromatic hydrocarbons in aqueous micellar solutions, *Chem. Phys. Lett.*, 1977, **51**(3), 501–505.

63 M. Kasha, H. R. Rawls and M. Ashraf El-Bayoumi, The exciton model in molecular spectroscopy, *Pure Appl. Chem.*, 1965, **11**(3–4), 371–392.

64 J. A. Halstead, Teaching the Spin Selection Rule: An Inductive Approach, *J. Chem. Educ.*, 2013, **90**(1), 70–75.

65 Z. E. X. Dance, S. M. Mickley, T. M. Wilson, A. Butler Ricks, A. M. Scott, M. A. Ratner and M. R. Wasielewski, Intersystem Crossing Mediated by Photoinduced Intramolecular Charge Transfer: Julolidine Anthracene Molecules with Perpendicular Systems, *J. Phys. Chem. A*, 2008, **112**(18), 4194–4201.

66 Y. Dong, A. A. Sukhanov, J. Zhao, A. Elmali, X. Li, B. Dick, A. Karatay and V. K. Voronkova, Spin–Orbit Charge-Transfer Intersystem Crossing (SOCT-ISC) in Bodipy-Phenoxazine Dyads: Effect of Chromophore Orientation and Conformation Restriction on the Photophysical Properties, *J. Phys. Chem. C*, 2019, **123**(37), 22793–22811.

67 F. Plasser, TheoDORE: A toolbox for a detailed and automated analysis of electronic excited state computations, *J. Chem. Phys.*, 2020, **152**(8), 084108.